Journal of Materials Chemistry A

ROYAL SOCIETY OF CHEMISTRY

PAPER

View Article Online
View Journal

Cite this: DOI: 10.1039/d5ta09250g

Unveiling the irreversible structural evolution upon rehydration of manganese-based Prussian white: an *in situ* X-ray diffraction study

Léna Pineau,[a] David Peralta,[a] Irina Profatilova,[a] Yohan Biecher,[a] Quentin Jacquet,[b] Sandrine Lyonnard,[b] Jakub Drnec,[c] Valentin Vinci[c] and Loïc Simonin *[a]

Manganese-based Prussian White (PW) $Na_{2-x}Mn[Fe(CN)_6]_y\cdot\square_{1-y}\cdot zH_2O$ ($0 \le x \le 2$, $0 \le y \le 1$) is a promising cathode material for sodium-ion batteries, due to the variety of its composition, its intercalation properties, and its good electrochemical performance. However, water-induced structural transformations limit its practical application and remain poorly understood. To unravel how water content governs structure transformations in relation to electrochemical performance, a rehydration of a heat-treated $Na_{1.67}Mn[Fe(CN)_6]_{0.88}\cdot\square_{0.12}$ compound was monitored by *in situ* synchrotron X-ray diffraction performed under a controlled atmosphere. At a dew point of −8 °C and a flow rate of 30 mL min^{-1}, the original rhombohedral (dehydrated) phase transforms in 20 minutes into a newly formed disordered monoclinic structure. Water uptake induces a significant expansion of the lattice volume and enhanced structural disorder. Regarding the electrochemical performance, a promising first discharge capacity of 145 mAh g^{-1} is obtained for the dehydrated PW, corresponding to 85% of its theoretical capacity (~170 mAh g^{-1}). Surprisingly, the rehydrated compound demonstrates a rather high capacity retention of 64%, while the hydrated compound retains only 14% of its initial capacity over 100 cycles at a C/10 rate in a voltage range of 2.5–4 V *vs.* Na^+/Na. This study provides new quantitative insights into the impact of humidity exposure on PW and on its structural integrity after a heat treatment. The present work will help implement cost-effective PW cathode materials in practice.

Received 13th November 2025
Accepted 17th April 2026

DOI: 10.1039/d5ta09250g

rsc.li/materials-a

1. Introduction

Li-ion batteries (LIBs) have dominated the market since their first commercialisation in 1991 thanks to their good performance in terms of energy density, cycle life and energy efficiency. However, a large amount of critical raw materials is generally needed in LIB manufacturing (Li, Ni, Co, Cu, *etc.*) which results in high commercialisation costs and could lead to geopolitical tension in the coming years.[1] Therefore, a promising solution is to design new battery systems composed of earth abundant elements in order to reduce the production cost below $100 per kWh by delivering the same amount of energy as current LIBs.[2,3] Substituting lithium, cobalt and nickel with more earth-abundant elements such as sodium, iron and manganese (*e.g.* sodium represents ~2.6% of the earth's crust and 3.3% in seawater) will allow for a considerable decrease in battery cost.[2] Moreover, replacing copper current collector (a critical raw material in LIBs) with aluminium is feasible in SIBs, as sodium does not form an alloy with aluminium. From this point of view, since the late 2000s, there has been a renewed interest in the sodium-ion battery technology (SIBs).[4] Nevertheless, the resulting energy density of SIBs is still lower compared to that of lithium battery technology and, therefore, higher energy density cathodes are required.

Prussian blue analogues (PBAs) are promising cathode materials for SIBs. Their theoretical gravimetric energy density are competitive with those of some Li-ion cathode materials such as $LiFePO_4$ (LFP) (*e.g.* 578 Wh kg^{-1} for $Na_2MnFe(CN)_6$ as compared with 595 Wh kg^{-1} for LFP).[5,6] PBAs have the following general chemical formula: $A_xMa[Mb(CN)_6]_y\cdot\square_{1-y}\cdot zH_2O$. A is an alkaline earth or alkali metal (generally Na, K or Li) and Ma and Mb are Transition Metal (TM) cations (often Fe or Mn) linked together by CN groups.[2] These materials consist of a three-dimensional network composed of MaN_6 and MbC_6 octahedra.[2] PBA compounds are classified into three categories, depending on the amount of Na introduced in the lattice and hence the oxidation state of the transition metals. The Berlin Green (BG) material is completely oxidized and thus desodiated, Prussian Blue (PB) is partially reduced and thus sodiated and Prussian White (PW) is completely reduced and thus contains

[a]Université Grenoble Alpes, CEA, LITEN, 17 Avenue des Martyrs, Cedex 9, Grenoble 38054, France. E-mail: lena.pineau@cea.fr
[b]Univ. Grenoble, Alpes, CEA, CNRS, Grenoble INP, IRIG, SyMMES, F-38000 Grenoble, France
[c]ESRF, ID31, 71 Avenue des Martyrs, 38000 Grenoble, France

two sodium atoms in its theoretical formula ($Na_2Ma[Mb(CN)_6]_y\cdot\square_{1-y}\cdot zH_2O$).[7–9] The PB compound originally contains only Fe atoms in its structure and is generally referred to as having an Fe–Fe composition. However, substitution of Fe in the Ma sites by other TMs such as Mn or Cu can occur, leading to Mn–Fe or Cu–Fe compounds, respectively.[10–13]

PW materials are very promising cathode materials due to the diversity of composition depending on synthesis conditions and their high specific capacity (theoretical capacity of ~170 mAh g^{-1} at 3.5 V *vs.* Na^+/Na).[6] Moreover, the material production is based on simple and safe synthesis protocols (aqueous synthesis without excessive energy-consuming processes or use of toxic solvents) relying on abundant elements that crystallise in a structure favourable for Na^+ intercalation.

However, numerous technical barriers impede wide commercialization of SIBs with PW-based cathodes. One of the main challenges is a deep understanding of changes in the crystallographic structure depending on several critical parameters. For example, the amount of water has a great influence on the structure of the material and, thus, the electrochemical properties. It is known that a significant amount of water in the form of surface water, interstitial water, or coordinated water can be present in the structure and may exceed 20% of its total mass after synthesis.[2,14,15] Coordinated water molecules are linked to the transition metal cyanide network and fill $M_b(CN)_6$ vacancy defects, generally represented by a lack of ferrocyanide anion $[Fe(CN)_6]^{4-}$ in the lattice.[2,3,10,14,16] From this point of view, the coordinated water content highly depends on the synthesis conditions as these greatly influence the formation of $Fe(CN)_6$ vacancies.[2] This coordinated water cannot be removed by heat treatment as temperatures exceeding the PBA's decomposition temperature (higher than 200 °C) would be needed, unlike interstitial or adsorbed water which is more weakly bound and thus easier to remove.[14,17,18] Interstitial water occupies the Na^+ vacancies, while the adsorbed water only interacts physically with the crystal surface. The interstitial and adsorbed water amounts are also determined by the synthesis conditions.[12,14,16] Hence, the presence of interstitial water also affects the crystallographic structure. Besides inducing structural changes, the water molecules can slow down the reaction kinetics during cycling by hindering Na^+ migration. Additionally, water can cause a lower coulombic efficiency due to side reactions during charging up to 3.8 V.[11,19,20] It is therefore important to understand simultaneously how water content modifies the crystal structure and impacts the electrochemical performance.

The role of interstitial water and its influence on electrochemical performance has been deeply studied for Fe–Fe compounds.[3,4,21–23] PBAs containing manganese (Mn) as transition metals (Mn–Fe compounds) have been extensively studied because they reveal a higher average operating potential (3.5 V) than Fe–Fe compounds (3.2 V).[3,4,10,24] The fully sodiated PW compound ($Na_2Mn^{II}[Fe^{II}(CN)_6]\cdot\square_{1-y}\cdot zH_2O$) exhibits a monoclinic structure in the presence of interstitial water. Song *et al.* studied the effect of interstitial water on the crystal structure and electrochemical performance in a $Na_{2-\delta}MnFe(CN)_6\cdot zH_2O$ compound. They reported a $P2_1/n$ space group for an air-dried PW sample while observing a $R\bar{3}$ space group for a vacuum-dried PW sample. Both samples were dried at 100 °C.[10] Similarly, most studies agree that hydrated PW adopts a monoclinic $P2_1/n$ structure, whereas the dried form exhibits a rhombohedral $R\bar{3}$ structure.[11,19,24,25] Furthermore, several studies have already reported the influence of rehydration on the dehydrated PW structure. Under air exposure, the rhombohedral structure evolves back to a monoclinic one by capturing H_2O molecules inside the lattice (interstitial water).[15,18,24,26,27] For example, Hartmann *et al.*[15] studied chemical and structural changes under humidity exposure of a PBA compound $Na_{1.8}Mn_{0.8}Fe_{0.2}[Fe(CN)_6]_{0.9}\cdot zH_2O$. This material exhibits a rhombohedral structure after a drying process at 150 °C and converts back to the monoclinic structure upon humid air exposure with slightly broader peaks than the cubic phase from a pristine sample $Na_{1.3}Mn_{0.8}Fe_{0.2}[Fe(CN)_6]_{0.9}\cdot zH_2O$. More recent reports considered the structural behaviour of dried samples under ambient air. Wang *et al.* studied structural characteristics of a $Na_{2-x}Mn_{0.8}Fe_{0.2}[Fe(CN)_6]_y\cdot nH_2O(0\le x\le 2, 0\le y\le 1)$ compound during the dehydration and rehydration processes and quantified the correlation among water content, structure, defects, and electrochemical properties. Using ICP and elemental analyses, they showed that $[Fe(CN)_6]$ defects significantly increase during a dehydration process, accompanied by structural damage.[18] Moreover, Clavelin *et al.* examined the dehydration and rehydration processes of a PW $Na_{1.87}Mn[Fe(CN)_6]_{0.99}\cdot 1.99H_2O$ sample synthesized by an aqueous co-precipitation method. They studied the rehydration of a dehydrated sample vacuum-dried at 150 °C for 20 h (20 mbar). They found a rhombohedral structure evolving under air exposure into a monoclinic phase in about 30 min for compact powder and less than 5 min for an electrode.[24] In a recent report, Li *et al.*[27] synthesized a $Na_{1.95}Mn[Fe(CN)_6]_{0.91}\cdot\square_{0.09}\cdot 0.08H_2O$ compound and demonstrated a fast re-absorption of water under ambient conditions, converting a rhombohedral phase back to a monoclinic phase. Considering the fast kinetics of the process, accurate monitoring under laboratory conditions is challenging, as it requires fast scanning techniques to capture transient features with sufficient angular resolution. Therefore, despite the large volume of re- and de-hydration research carried out on PW materials, a deeper understanding of the structural evolution under controlled water uptake of dehydrated MnFe through the analysis of the phase content evolution is required. This work aims to track the details of the insertion of water molecules into the lattice precisely and in real time and evaluate how their content and type affect electrochemical performance.

Herein, we report a PW compound $Na_{1.67}Mn[Fe(CN)_6]_{0.88}\cdot\square_{0.12}\cdot 2.5H_2O$ synthesized using a precipitation method from $Na_4Fe(CN)_6\cdot 10H_2O$ and $Mn(NO_3)_2\cdot 4H_2O$ precursors. After drying at 180 °C under high vacuum (10^{-2} mbar), the material adopts a rhombohedral $R\bar{3}$ phase, as shown by XRD. The material structure evolution is followed under exposure to the atmosphere with controlled humidity by time-resolved synchrotron *operando* X-ray diffraction (SXRD). Infrared spectroscopy, thermogravimetric analyses and Mössbauer analyses are used to assess the influence of water content on physico-

chemical properties of the material. A reversible cycle of water desinsertion–insertion was observed at a local scale; however an irreversible phenomenon occurs at the particle scale regarding the difference in lattice parameters. Galvanostatic cycling is compared for hydrated, dehydrated and rehydrated $Na_{1.67}Mn[Fe(CN)_6]_{0.88}\cdot\square_{0.12}\cdot 2.5H_2O$ samples after ambient air exposure. A promising first discharge capacity of 145 mAh g^{-1} for the dehydrated PW is obtained. A surprising capacity retention of 64% is obtained for the rehydrated compound over 100 cycles at a C/10 rate *vs.* Na^+/Na, while the hydrated compound retains only 14% of its initial capacity.

2. Methods

2.1. Material synthesis

All the samples were synthesized by using commercial reactants: sodium ferrocyanide decahydrate (Sigma Aldrich®, $Na_4Fe(CN)_6\cdot 10H_2O$, 99%), manganese nitrate tetrahydrate (Sigma Aldrich®, $Mn(NO_3)_2\cdot 4H_2O$, 97%), and sodium citrate tribasic dihydrate (Sigma Aldrich®, $C_6H_5Na_3O_7\cdot 2H_2O$, 99%). All reactants were used without further purification. The synthesis of PW, $Na_{2-x}Mn[Fe(CN)_6]_y\cdot\square_{1-y}\cdot zH_2O$, was carried out by a simple precipitation method (Fig. S1). Specifically, a solution of 250 mL of $Na_4Fe(CN)_6\cdot 10H_2O$ (15 g) was prepared and introduced in a reactor. A second solution of 750 mL of $Mn(NO_3)_2\cdot 4H_2O$ (8 g) and sodium citrate (65 g) was prepared in a bottle. The second precursor's solution was introduced in the reactor under stirring at 1000 rotations per minute (rpm). The synthesis was achieved when the second solution was completely introduced into the reactor. The obtained solution was left to age for 16 hours at room temperature. The obtained precipitate was washed three times with deoxygenated water and placed under vacuum at room temperature overnight. After being ground in a mortar, the as-prepared compound is denoted as MnPW-H, where H refers to hydrated. Then, MnPW-H powder was dried under strong vacuum (10^{-2} mbar) at 180 °C for 16 hours with a ramping rate of 6 °C min^{-1} to obtain a dehydrated powder MnPW-D (D refers to dehydrated). MnPW-R (R refers to rehydrated) was denoted as MnPW-D exposed to ambient air. All samples' descriptions are summarized in Table 1.

2.2. Synchrotron X-ray diffraction under a humidity-controlled atmosphere

Synchrotron *in situ* X-ray diffraction (SXRD) patterns were collected at the ID31 beamline of the European Synchrotron Radiation Facility (ESRF) in Grenoble, with an energy of 75 keV. The X-ray beam size was 200 μm vertically and 400 μm horizontally. The measurements were conducted between 1.2° and 24.6 by packing about 5 mg of powder into 4 mm outer diameter (O.D.) and 2.04 mm inner diameter (I.D.) quartz glass capillaries. The capillary was loaded with the powder and tightly closed in an Ar-filled glove box (O_2 and H_2O concentrations less than 0.1 ppm). Then, the sample was transferred to the beamline and connected to the gas line. The *in situ* rehydration was performed using a home-made test assembly built around the beamline. Argon carrier gas was supplied at a flow of 30 mL min^{-1} and humidified at a dew point of −8 °C using a Cellkraft® humidifier. After being humidified, Ar flow was forced through the airtight capillary containing the dehydrated powder MnPW-D. SXRD patterns were acquired every 7 s. The air tightness of the capillary was ensured using Swagelok® connections with Teflon® gaskets in contact with the glass cell to prevent damage. A system of automatic valves was used to control the gas flow remotely. The data can be found at https://doi.org/10.15151/ESRF-ES-1901542848.

Furthermore, *ex situ* measurements were conducted at the beamline on pristine powder (MnPW-H) and rehydrated powder after one day under air-exposure (MnPW-R). The measurements were conducted between 0.1° and 17.1° with an energy of 75 keV. Identical capillaries were used and loaded with approximately 5 mg of powder at ambient air.

All selected diffractograms were refined by the Rietveld method using Fullprof WinPLOTR.

2.3. Laboratory X-ray diffraction

X-ray diffraction (XRD) experiments were performed on a Bruker Advance X-ray diffractometer, equipped with a Cu target X-ray (1.54056 Å) between 8° and 70°. These measurements were only conducted on rehydrated powders (MnPW-R, MnPW-R2 and MnPW-R3).

2.4. Elemental analysis

Elemental analysis was performed by ICP-OES measurements on the PW powders after synthesis. The samples were dissolved by microwave digestion with a mixture of HNO_3, HCl and HF acid. The mineralization was complete.

The water content of the electrodes was quantified using a Karl Fischer moisture titrator (Metrohm).

2.5. Fourier transform infrared (FTIR) spectroscopy

FTIR experiments were performed to confirm the structure of the samples and the presence of water, on a Thermo Scientific Nicolet iS50. The measurements were carried out with

Table 1 Sample nomenclature

Sample name	Description	Comments
MnPW-H	Hydrated	As-synthesized compound
MnPW-D	Dehydrated	As-synthesized compound dried at 180 °C under vacuum
MnPW-R	Rehydrated	Dried compound exposed to ambient air for 24 h

a diamond crystal Attenuated Total Reflectance (ATR) accessory. The samples were analysed in air and under argon in a sealed cell for the hydrated samples (MnPW-H and MnPW-R) and the dried sample (MnPW-D), respectively. Both samples were analysed between 400 cm^{-1} and 4000 cm^{-1}.

2.6. Thermal analysis

The thermal evolution and the water content of the material were observed with thermogravimetric analysis (TGA). The data were collected on a TGA550 model from the Waters SAS company under argon with a constant heat ramp rate of 10 °C min^{-1} until a final temperature of 550 °C. The samples were measured in sealed aluminium crucibles.

2.7. Morphology and particle size distribution

The particle morphology was observed by Scanning Electron Microscopy (SEM, Zeiss Sigma 300), with an operating voltage of 5 kV. The particle size distribution was determined on a laser diffraction particle size analyser from the Anton Paar company. The measurements were performed in water solvent after 10 minutes under ultrasound.

2.8. Mössbauer spectroscopy

Mössbauer spectroscopy was performed on hydrated samples (MnPW-H and MnPW-R) and dried samples (MnPW-D). Mössbauer spectra were recorded at room-temperature on a home-made spectrometer operating in a constant acceleration mode in transmission geometry. The analysis velocity was ranging between −6 and +6 mm s^{-1}. They were analysed with WMOSS software (WMOSS4 Mössbauer Spectral Analysis Software, https://www.wmoss.org, 2009–2016). The isomer shifts are referenced against that of metallic iron foil at room-temperature.

2.9. Electrochemical tests

All electrodes were manufactured using an organic-based formulation. The positive electrode slurry was prepared by mixing 70 wt% of active material PW $Na_{2-x}MnFeCN_6$, 20 wt% of Super C65 carbon black and 10 wt% of polyvinylidene fluoride (PVDF) as a binder. *N*-Methyl-2-pyrrolidone (NMP) was used to adjust the viscosity of the slurry. The latter was coated on aluminium foil with a thickness of 100 μm and dried at 55 °C overnight for the hydrated and rehydrated powder. Before transferring it into the glovebox in order to prepare coin cells, the electrodes from the hydrated and rehydrated powder were dried at 80 °C. The electrode preparation process for the dried powder was carried out in a glovebox, and the slurry was dried in a vacuum oven. All electrodes were punched out with a diameter of 14 mm and calendared at a pressure of 1 ton. The mass loading of the electrode active material was about 1 mg cm^{-2}.

The electrochemical half-cells were assembled in an argon-filled glovebox. Half cells were assembled with a PW positive electrode, one glass fibre filter paper (Whatman GF/D) separator, and a negative electrode of Na metal for all coin cells. The electrolyte was composed of 1 mol L^{-1} of $NaPF_6$ dissolved in ethylene carbonate (EC) and dimethyl carbonate (DMC) with a volume ratio of 50 : 50 mixed with 2 wt% of fluoroethylene carbonate (FEC). The electrochemical test for the charge–discharge cycles was carried out in 2032-type coin cells, using an Arbin battery testing system. The galvanostatic tests were performed in a voltage range of 2.5–4 V (*vs.* Na^+/Na), with a C-rate of C/10. The specific capacities and the current rate are calculated based on a theoretical capacity of 171 mAh g^{-1} for $Na_2Mn[Fe(CN)_6]$. All electrochemical tests were performed at 25 °C. The Galvanostatic Intermittent Titration Technique (GITT) and Electrochemical Impedance Spectroscopy (EIS) were performed on a Biologic battery testing system. The GITT was applied using a C-rate of C/10 in the voltage range from 2.5 to 4.0 V (*vs.* Na^+/Na), with 5 cycles performed at each C-rate. The half-cell was alternately charged for 10 min at a current density of 20 mA g^{-1} followed by 120 min of rest and then discharged in the same way. The procedure was repeated for the full voltage range of operation. The Na^+ diffusion coefficient (D_{Na^+}) was calculated by using simplified eqn (1), based on Fick's second law:[19]

$$D_{Na^+} = \frac{4}{\pi\tau}\left(\frac{nV}{S}\right)^2\left(\frac{\Delta E_s}{\Delta E_\tau}\right)^2 \quad (1)$$

where n and V represent the molar mass (mol) and the molar volume (cm^3 mol^{-1}) of the MnPW material, respectively. τ signifies the time duration of a current pulse, and S is the geometrical surface of the positive electrode. ΔE_τ represents the voltage variation caused by charging/discharging in a single-step GITT process, and ΔE_s is the equilibrium voltage variation during a current pulse in two adjacent GITT processes.

The EIS was examined before cycling, after one cycle, and after 5 cycles. The frequency range was set from 1000 MHz to 10 000 mHz, with an applied amplitude of 20 mV.

3. Results and discussion

3.1. Structure of the hydrated compound

MnPW-H was prepared by a precipitation synthesis method and characterized in this initial section. SXRD analysis was first carried out. The pattern is shown in Fig. 1(a) and vertical lines indicate characteristic peaks for the monoclinic $P2_1/n$ phase, space group $P2_1/n$, confirming a well-crystallized structure and a pure phase, as already observed in the literature.[10,11,24] The lattice parameters and the atomic positions were refined by the Rietveld method. The values of the lattice parameters are as follows: a = 10.582(1), b = 7.555(1), c = 7.382(2) Å, and β = 92.03(3)°. The atomic positions are shown in Table S1 in the SI. SEM on MnPW-H was carried out and the obtained images are shown in Fig. 1(b). Cubic-shaped primary particles are observed, with a typical size of around 4 μm. This average size was confirmed by the laser diffraction technique (Fig. S2 and Table S2). In order to confirm the presence and quantify the amount of water in the hydrated sample, TGA and ATR-FTIR analyses were performed on MnPW-H (Fig. 1(c) and (d)). The TGA analysis exhibits three distinct weight losses from 0 °C to 160 °C, from 160 °C to 210 °C and from 320 °C to 380 °C. According to several publications, the first loss, up to 160 °C,

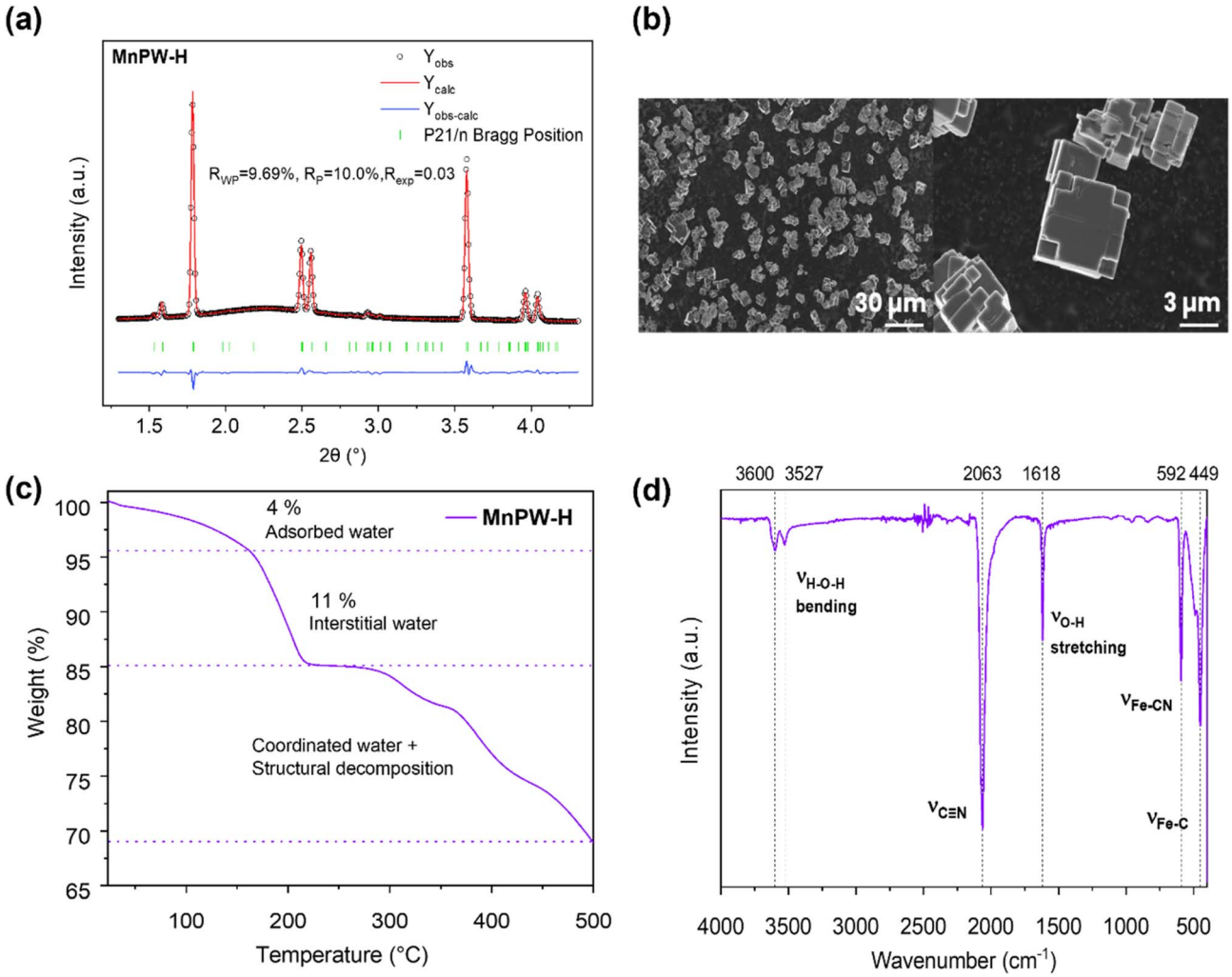

Fig. 1 Properties of the pristine material: SXRD pattern (a), SEM observations (b), TGA analysis at 10 °C min^{-1} under an argon atmosphere until 500 °C (c) and ATR-FTIR measurements (d) of the hydrated powder MnPW-H.

can be assigned to adsorbed water, while the second step corresponds to interstitial water. The last step can be attributed to the decomposition of the structure.[10,24] A weight loss of 4% of adsorbed water and 11% of interstitial water can be seen. Assuming that the material is dehydrated after removing adsorbed and interstitial water, it can be deduced that at least 2.5 molecules per unit formula of H_2O are present in the material, considering that the dehydrated molar mass (280 g mol^{-1}) corresponds to 86% of the total mass. Then, ATR-FTIR spectra show two peaks at 3600 cm^{-1} and 3527 cm^{-1} and one sharp peak at 1617 cm^{-1}, corresponding to H–O–H bending and O–H stretching, respectively. The first H–O–H bending at 3600 cm^{-1} is characteristic of adsorbed water, while the other two peaks confirm the presence of interstitial water in the structure, as described by Song *et al.*[10] Sharp peaks at 592 cm^{-1} and 449 cm^{-1} are indexed to be Fe–CN and Fe–C bonds, respectively. The most intense peak at 2063 cm^{-1} is attributed to the C≡N triple bond.[10,28] The sample elemental composition was determined by ICP-OES analysis (Table S3). From this analysis, we could determine the experimental anhydrous formula to be $Na_{1.67}Mn[Fe(CN)_6]_{0.88}\cdot\square_{0.12}$. Finally, according to the TGA and ATR-FTIR analyses, the final formula of the sample would be $Na_{1.67}Mn[Fe(CN)_6]_{0.88}\cdot\square_{0.12}\cdot 2.5H_2O$.

As mentioned above, the dehydrated sample transforms its rhombohedral structure $R\bar{3}$ into a monoclinic under air exposure.[15,24,26] Hence, MnPW-H was dried under vacuum (10^{-2} mbar) at 180 °C to become MnPW-D.

3.2. *In situ* rehydration study by SXRD

The structural parameter evolution of the MnPW-D sample exposed to humidity is described in this following analysis. In order to follow the evolution of the material's structure during its rehydration under a humidity-controlled atmosphere (dew point of −8 °C) with high resolution, synchrotron patterns were collected at the ID31 beamline of the ESRF in Grenoble, with an energy of 75 keV. A quartz glass capillary filled with the powder sample was purged with humid argon. *In situ* SXRD profiles of the water uptake of the dehydrated material MnPW-D are shown in Fig. 2(a). The 011 reflection peak from the monoclinic $P2_1/n$ phase and the 012 reflection peak from the rhombohedral

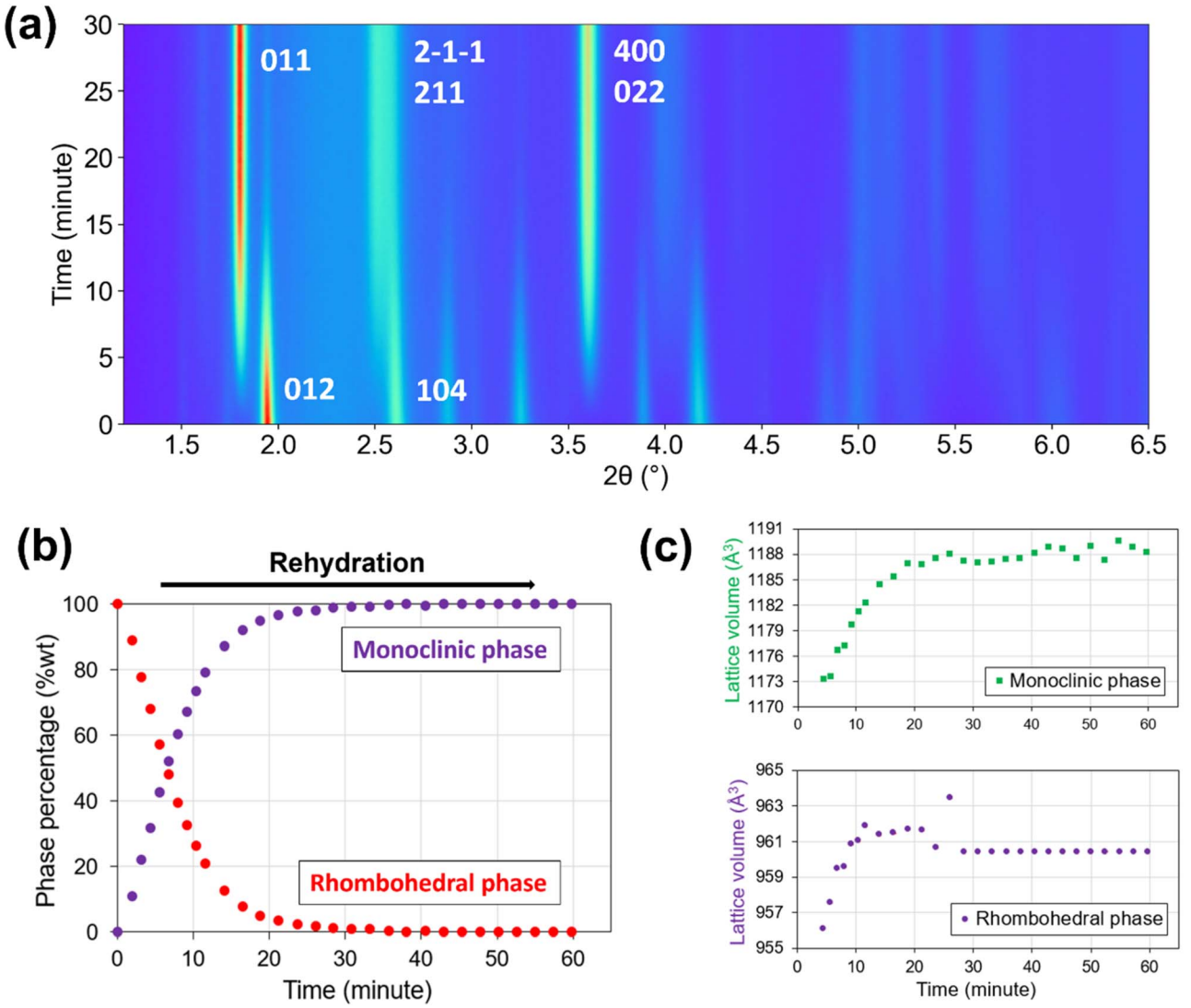

Fig. 2 Structural parameter evolution during rehydration: *in situ* XRD measurements as a function of humidity-controlled atmosphere exposure of dried sample MnPW-D (a), evolution of the rhombohedral (red dots) and the monoclinic phase (purple dots) depending on the time exposure at a dew point of −8 °C and with a flow rate of 30 mL min^{-1} (b), and evolution of the lattice volume of the monoclinic cell (green marker) and the rhombohedral cell (purple marker) during the rehydration (c). The lattice volume of the monoclinic and rhombohedral cells is normalized in the cubic cell.

$R\bar{3}$ phase appear respectively at 1.25° and 1.3°. We can observe that MnPW-D transforms into the monoclinic phase ($P2_1/n$) in the first minutes of the experiment. Rietveld refinements were performed on the 30 different scans presented in Fig. S3–S5, from 0 to 60 minutes. The correlation table between the scan number and the time in minutes is presented in Table S4 (SI). The first scan (Scan 0) and the last scan (Scan 29) correspond to $T = 0$ minute and $T = 1$ hour, respectively. Using the Rietveld refinement data allows obtaining a quantitative phase ratio for all scans (Fig. 2(b)). The evolution of the rhombohedral and the monoclinic phase percentage depending on the time exposure reveals a rapid rehydration up to 95% in less than 20 minutes. Moreover, the two phases co-exist at almost 50% after the exposure to humid argon for 7 minutes. As observed in previous studies, the intensity of the characteristic 011 peak of the monoclinic $P2_1/n$ phase is rising from the first scan until the last one, while the rhombohedral phase is diminishing with the rising amount of water molecules from the humid air.[18,24,26,27] Clavelin *et al.* showed a dehydrated rhombohedral structure evolving under laboratory ambient air exposure into a monoclinic structure in about 30 min for compact powder and less than 5 min for an electrode.[24] Faster kinetics of rehydration is observed in the present study possibly due to the fact that the argon flow was forced through the capillary, while the hydration reaction was limited by diffusion of humidity from the ambient air in work.[24] Additionally, different rehydration mechanism hypotheses in adsorption kinetics may be highlighted: first, the water insertion into the most accessible interstitial sites, associated with the water adsorption at the surface and then the water transfer from the surface to the interstitial sites. After 20

minutes, the rehydration process presents lower kinetics. The water transfer may be impeded with time upon filling the reactive sites.

Tables S5–S34 show all refinement parameters of the 30 refined scans from the SXRD experiment. Scans 1 to 29 were refined with 2 phases (space groups $R\bar{3}$ and $P2_1/n$), while scan 0 was only refined in the $R\bar{3}$ space group, corresponding to the MnPW-D sample. These two phases co-existed from the first minutes until the end of the experiment after one hour, according to the observation of the XRD profile shown in Fig. S3–S5. Fig. 2(b) shows that the percentage value of the rhombohedral $R\bar{3}$ phase reaches 0% with Rietveld refinement within one hour. However, the refinement of scan 29 shows that characteristic 012 peak of the dehydrated phase is still visible in a very low quantity, even after one hour of exposure to humid argon (Fig. S5). The Rietveld refinement method would not quantify the residual phase percentage. The residual rhombohedral phase observed after 1 hour under humidity exposure is in line with the work by Li *et al.*[27]

The lattice volume evolution of the monoclinic and rhombohedral phases during the rehydration process was followed (Fig. 2(c)). To ensure an accurate comparison, the lattice volume of the monoclinic and the rhombohedral unit cells (V_C and V_R) were converted into a cubic-based one (V_C). The volume is normalized in the cubic cell by using the following equations:[29]

$$V_C = V_M \frac{(b_M{}^2 + c_M{}^2)}{b_M c_M \sin\beta}$$

$$V_C = V_R \frac{4}{3}$$

A slight increase of the lattice volume in the first 20 minutes reveals an expansion of the lattice volume during the rehydration ($\approx$15 Å^3 for the monoclinic cell and $\approx$5 Å^3 for the rhombohedral cell). Xiao *et al.* evidenced that the dehydration process induced stronger d–π interactions between Na and N by removing the water molecules and hence reducing the volume of the structure.[30] During the rehydration process, water molecules reinsert into the lattice and may cause the opposite effect with an increase of the lattice volume. The increase of water molecule content is confirmed by the evolution of the water occupancy in the monoclinic phase during the *in situ* rehydration experiment (Fig. S6). Furthermore, as seen in the same figure, the rehydrated powder reveals a different monoclinic phase from the pristine one. The latter exhibits thinner peaks with an average Full Width at Half Maximum (FWHM) of 0.0259° and 0.0497° for the rehydrated powder. Furthermore, Wang *et al.* demonstrated that the dehydration process induced an increase of the [Fe(CN)$_6$] vacancy defects, from 4% to 8% at 190 °C.[18] The increase of FWHM observed for the rehydrated sample could probably occur during the dehydration process. Indeed, the dehydrated phase exhibits broad peaks (Fig. S3(a)), suggesting the creation of a structural disorder during the dehydration step.

In order to study the complete rehydration of the sample, a dehydrated sample was exposed to ambient air for 24 hours. The resulting sample is referred to as MnPW-R.

3.3. Influence of the interstitial water on PW's properties

Physical and electrochemical characterization studies were performed on MnPW-H, MnPW-D, and MnPW-R to clarify the impact of interstitial water on the material properties. First, *ex situ* SXRD analyses were additionally performed on MnPW-R (Fig. S7). The crystal structure of MnPW-R is monoclinic in the $P2_1/n$ space group. The MnPW-R pattern was refined by the Rietveld method, confirming the space group $P2_1/n$ with a = 10.584(2), b = 7.643(3), c = 7.304(3) Å, and β = 91.60(2)°. Table S35 shows the refinement parameters of the MnPW-R sample from an *ex situ* SXRD analysis. The observed pattern indicates that the rehydration is complete since the rhombohedral 012 peak at 1.9° totally disappears. The MnPW-R *ex situ* SXRD pattern was compared to that of the MnPW-H sample in Fig. 3(a) and the lattice parameter comparison between MnPW-H and MnPW-R is shown in Fig. S8. A significant difference is observed for the *b*, *c* and beta parameters, while the *a* parameter exhibits similar values. However, the lattice volumes of MnPW-H and MnPW-R samples are close (588(1) Å^3 and 590(1) Å^3, respectively). This phenomenon could be explained by the opposite balance of *b* and *c* parameters in the lattice, with the *a* position remaining stable. The two peaks between 2.3° and 2.7° and between 3.8° and 4.2° are convoluted, which may be explained by the presence of broad peaks with an increase of the FWHM during the rehydration. This phenomenon can be attributed to the internal presence of residual strain or finer cracks. Beyond inducing internal structural changes at the crystal lattice scale, the incorporation of water could have an impact on particle morphology. Therefore, SEM observations were performed on the three samples (Fig. S9). Primary particle observations did not reveal major cracks on the dehydrated sample after the heat treatment at 180 °C under vacuum and reveal similar cubic shapes for the three samples. These observations would mean that heat treatment does not induce macroscopic alterations. Moreover, the hypothesis of a third phase could also be taken into consideration in MnPW-R. Notably, a cubic crystallographic structure was reported for the material containing a low Na$_x$ content (x < 1.5), caused in some cases by a high concentration of FeCN$_6$ vacancies.[10,11,25,31] Since we may have a lower amount of Na ions, a cubic phase could emerge between the convoluted double peaks with the loss of Na ions during the rehydration.[11,25,31] To evaluate this hypothesis, Mössbauer spectra were acquired on MnPW-H, MnPW-D and MnPW-R at 295 K (Fig. S10). All three samples show the same single peak, corresponding to a 100% Fe^{2+} component. Since a loss of Na ions induces oxidation of the transition metal (Mn or Fe), the possible loss of Na ions in the rehydrated material MnPW-R could be due to Mn oxidation. Hence, it would be interesting to perform XAS or XPS analyses in order to evaluate the oxidation state of Mn. To summarize, this rehydration phenomenon suggests an irreversible transformation considering the lattice parameters and a disordered

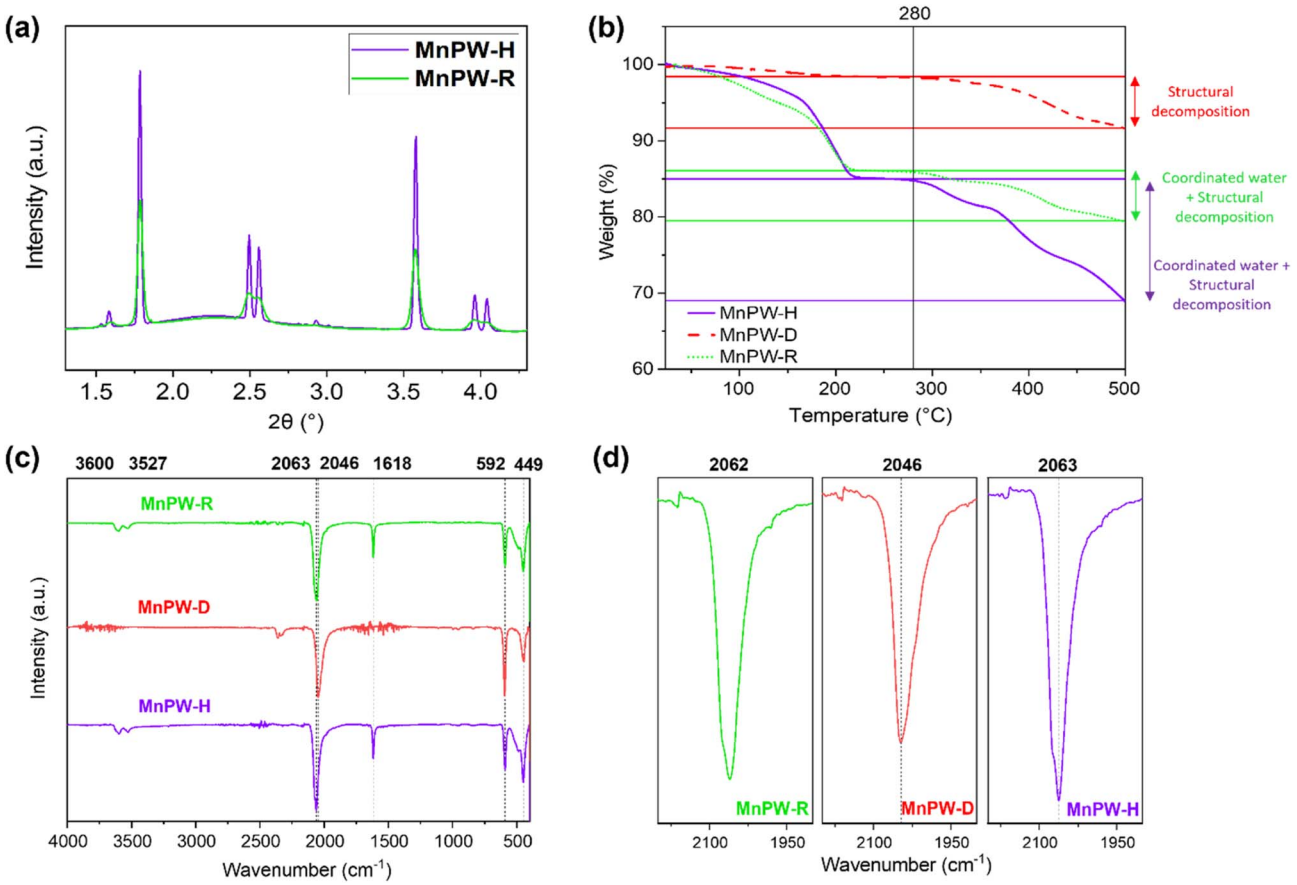

Fig. 3 Comparative properties of samples with differing water content: XRD patterns of MnPW-H (purple) and MnPW-R (green) (a), TGA analysis at 10 °C min^{-1} under an argon atmosphere until 500 °C (b), ATR-FTIR measurements (c) and zoom of C–N peaks (d) of MnPW-H, MnPW-D and MnPW-R.

monoclinic phase which presents a higher disorder than the as-synthesised one. Additionally, Tables S1 and S35 reveal similar oxygen occupancy and atomic positions, suggesting a reversible water molecule insertion–deinsertion process after 24 h under ambient air.

In order to highlight the differences in water content of the three samples, TGA was performed on MnPW-H, MnPW-D and MnPW-R (Fig. 3(b)). The MnPW-D TGA curve shows a lack of adsorbed and interstitial water in the structure. However, a residual water amount can be highlighted until 280 °C (≈2% of weight loss). MnPW-R exhibits three main weight losses, similarly to MnPW-H: the first between 0 and 150 °C corresponding to the adsorbed water, the second from 150 °C to 220 °C attributed to the interstitial water release and the third from 280 °C until 500 °C associated with structure decomposition.[10,24,32] The higher amount of adsorbed water in MnPW-R compared to MnPW-H is confirmed by the gradual weight decrease of about 6% up to 150 °C. Additionally, MnPW-R shows a slightly lower amount of water filling the interstitial sites (8%) compared to MnPW-H (11%). Globally, MnPW-R exhibits a total weight loss of 14% corresponding to approximately $2.3H_2O$ molecules per formula unit; hence it incorporates less interstitial water than the hydrated phase, although rehydration is complete (Fig. S7). Regarding the region above 280 °C, MnPW-D and MnPW-R exhibit similar weight losses at above 280 °C (around 7% weight loss). Regarding MnPW-R, two weight losses are visible: the first contribution is weak and may be due to a low quantity of re-inserted coordinated water, while the second predominantly arises from structural decomposition. Hence, after dehydration and rehydration, the weight losses are identical and correspond mainly to the structure decomposition because the coordinated water was removed.[33]

The existence and amounts of adsorbed and interstitial water were further confirmed by ATR-FTIR. Fig. 3(c) shows the typical water spectral features in MnPW-H, D and R samples. The comparison of characteristic peaks, *e.g.* O–H stretching and H–O–H bending (3600 cm^{-1} and 1618 cm^{-1}, respectively), reveals the removal of adsorbed and interstitial water in the structure with a lack of characteristic peaks in the MnPW-D spectrum. Similarly to MnPW-H, water characteristic peaks at 1620 cm^{-1}, 3527 cm^{-1} and 3600 cm^{-1} in the MnPW-R spectrum confirm the presence of adsorbed and interstitial water in the sample structure. Additionally, sharp peaks at 592 cm^{-1} and 449 cm^{-1} are indexed to be Fe–CN and Fe–C bonds, respectively, on the three sample profiles.[10] A residual peak attributed to ambient CO_2 is observed at 2350 cm^{-1} in the MnPW-D infrared spectrum. Although a background spectrum was recorded prior to the measurement, fluctuations in the atmospheric CO_2

concentration can still affect the result. Fig. 3(d) shows bond vibration evolution under air exposure through ATR-FTIR measurements. MnPW-D features a C≡N triple bond characteristic peak at 2046 cm^{-1} which shifted to a higher wavenumber (lower energy of the bond) after the dehydration process. The removal of water molecules may induce a change in the electronic environment of the C≡N bond with water molecules, indicated by a peak shift. It is also interesting to notice that the C≡N bond splits into at least two convoluted peaks during the rehydration of the sample in ambient air, similarly to the hydrated sample. Hence, a reversible phenomenon at the bond scale is observed from MnPW-H to MnPW-R sample curves.

So far, the rehydration process induced irreversible internal structural effects but a reversible water capture process through TGA analysis. To further understand the (ir)reversibility of water-induced transformations, structural evaluations after several dehydration and rehydration cycles are necessary. Two samples MnPW-D2 and R2 were prepared, respectively, *e.g.* MnPW-R is dehydrated at 180 °C under vacuum (D2) and then exposed again to ambient air for one day (R2). Another identical cycle yielded samples D3 and R3. The amount of water captured by these seven samples is first evaluated by TGA (Fig. S11(a)). MnPW-D, MnPW-D2, and MnPW-D3 TGA curves show a lack of adsorbed or interstitial water in the structure. A residual amount can still be observed at around 200 °C (≈2% weight loss). MnPW-R2 and MnPW-R3 exhibit three distinct weight losses, between 0 and 150 °C (adsorbed water), from 150 °C to 200 °C (interstitial water) and between 300 °C and 380 °C (removal of coordinated water and structure decomposition), similarly to MnPW-R.[10,24] Moreover, a slightly higher total weight loss of 13% is highlighted for both compounds, corresponding to $2.25H_2O$ molecules per formula unit, compared to MnPW-R. MnPW-R2 and MnPW-R3 curves exhibit a similar behaviour to MnPW-R, with a higher amount of adsorbed water and a lower amount of interstitial water, compared to MnPW-H.

Furthermore, the XRD analysis of the three rehydrated samples (Fig. S11(b)) exhibits similar XRD profiles for all rehydrated samples after one day, with peak width as broad as that of MnPW-R. The evolution of the normalized intensities is non-significant since the evolution is not linear. Hence, a structural transformation occurs during the first dehydration–rehydration cycle (MnPW-R), while the structure disorder remains stable over two additional cycles, and a similar amount of interstitial water is captured (MnPW-R2 and R3).

The rehydration process triggers an irreversible transformation, yielding a disordered monoclinic phase distinct from the as-synthesized material, as reflected in its modified lattice parameters. Additionally, FT-IR analyses highlight a reversible phenomenon at the bond scale while MnPW-R shows a lower amount of water filling the interstitial sites compared to MnPW-H.

3.4. Influence of water on electrochemical performance

The electrochemistry was studied to understand the influence of water molecules on the cycling performance. Fig. 4 shows sodium insertion and extraction behaviour through galvanostatic measurements of MnPW-H, MnPW-D and MnPW-R. The sodium half-cells were charged and discharged in CC–CV mode with a top-off voltage at 4 V. The first discharge capacity profile as a function of the potential (*vs.* Na^+/Na) is shown in Fig. 4(a) in a voltage range of $2.5\ V \leq V \leq 4\ V$ at a C-rate of 0.1C. MnPW-D exhibits a high first discharge capacity value of 145 mAh g^{-1} with an average potential of 3.5 V *vs.* Na^+/Na. Knowing that the sodium content of the material is 1.67, it is in good agreement with the theoretical capacity of 144 mAh g^{-1}. One plateau is observed for both charge and discharge of the MnPW-D sample, even though a second plateau can be observed at around 3.4 V during discharge, which may correspond to the deconvolution of the two reduction reactions of the manganese and then the iron.[2] MnPW-H and MnPW-R exhibit a moderate first discharge capacity of 112 mAh g^{-1} and 115 mAh g^{-1}, respectively. Two plateaus are observed for both charge and discharge of MnPW-H and MnPW-R samples, corresponding to the deconvolution of the Fe and Mn oxidation reactions.[2] However, the MnPW-H first charge cycle curve exhibits a second plateau at higher potential, resulting in higher polarization. In 2015, Song *et al.*'s study on the water content effect in a $Na_{2-\delta}MnFe(CN)_6 \cdot zH_2O$ compound highlighted the role of the $C{\equiv}N^-$ anion rotation on the energy difference in oxidation reactions. The dehydration process induces a rhombohedral structure, involving a shorter Mn···Fe distance in the structure lattice. Hence, the rotation of the linear $C{\equiv}N^-$ anions from the Mn···Fe axes becomes more constrained and induces a different response of the High Spin (HS) Mn^{2+}/Mn^{3+} and Low Spin (LS) Fe^{2+}/Fe^{3+}couples' energies.[10] This phenomenon would explain the potential difference of the Fe and Mn redox reactions between a hydrated and dehydrated compound.

Fig. 4(b) shows capacity retention of MnPW-H, MnPW-D, and MnPW-R between 2.9 V and 4.0 V *vs.* Na^+/Na. Surprisingly, MnPW-D and MnPW-R demonstrate similar capacity retentions, 61% and 64%, respectively. On the other hand, MnPW-H shows a very poor capacity retention of 14% after 100 cycles. As seen in Fig. 3(b), the MnPW-R powder ($2.3H_2O$) exhibits a slightly lower global water content than the MnPW-H powder ($2.5H_2O$). Since the electrodes were dried at 80 °C for 48 h under vacuum before assembling coin cells, a part of adsorbed water may be removed and lead to a higher retention capacity, enhanced by a lower amount of water filling the interstitial sites of MnPW-R (8%) compared to MnPW-H (11%). To determine the real water content before cycling, Karl Fischer measurements were performed on pristine electrodes dried at 80 °C before being transferred into the glovebox. An amount of 96 550 ppm and 64 698 ppm obtained for the MnPW-H and MnPW-R electrodes, respectively, confirms the lower interstitial water content in MnPW-R. One possible hypothesis might propose that the higher global water content in MnPW-H could explain the poorer capacity retention of this sample. However, the structure differences between these three samples must be taken into consideration. While MnPW-D has a capacity retention comparable to that of MnPW-R, both of the samples present a different structure, with a higher initial specific discharge capacity for MnPW-D. Moreover, as seen in Fig. 3(a),

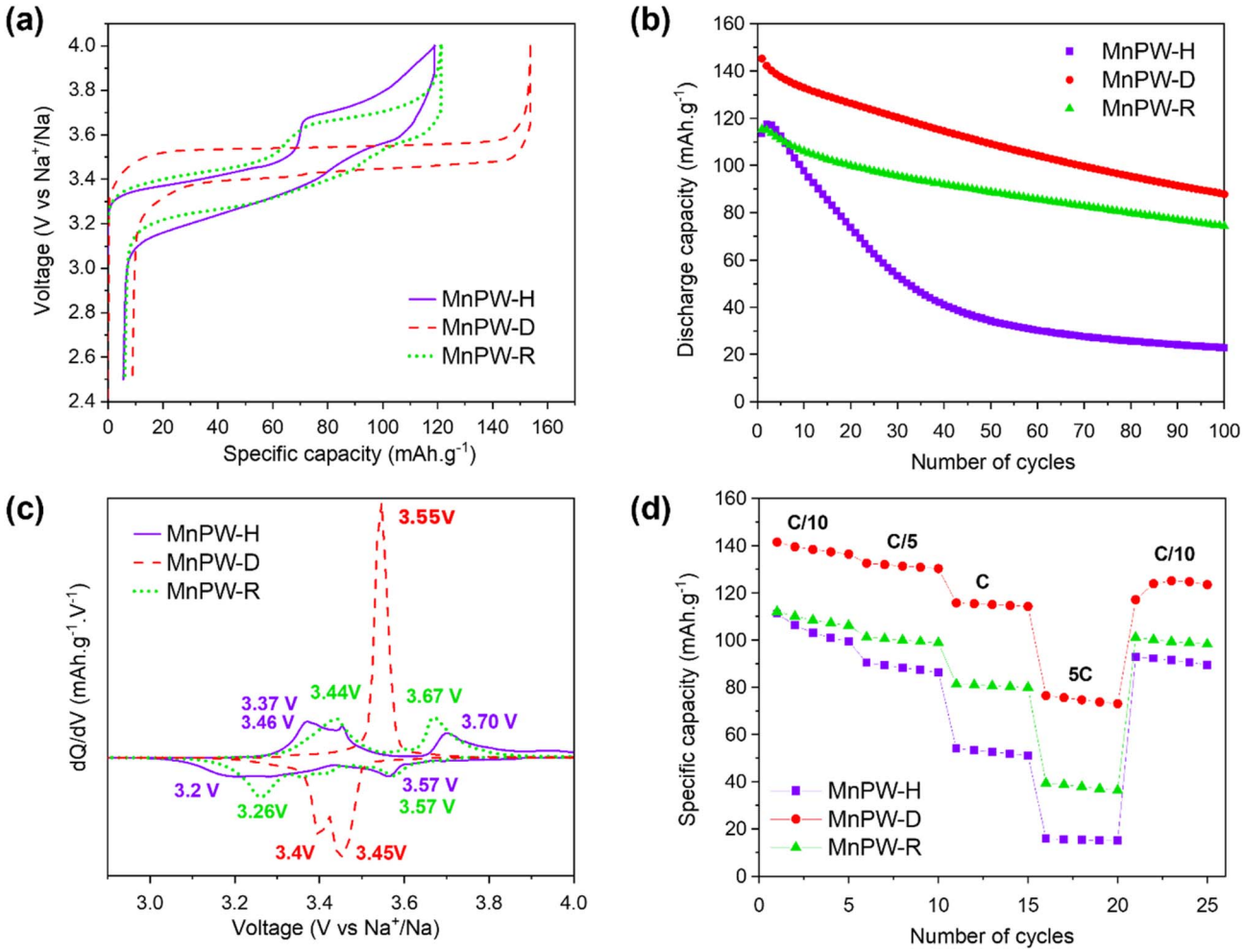

Fig. 4 Electrochemical performance of samples with different water contents: galvanostatic first charge and discharge curves (a), capacity retention over 100 cycles (b), dQ/dV curves (c), and rate capabilities (d) of MnPW-H (purple), MnPW-D (red) and MnPW-R (green) in a voltage range of 2.5 V ≤ V ≤ 4 V *vs.* Na^+/Na at a C-rate of 0.1C.

MnPW-R presents a disordered monoclinic phase with a higher disorder than the as-synthesised one. This rehydrated monoclinic phase with modified lattice parameters may lead to an alternative Na diffusion pathway in the structure and might explain the higher capacity retention compared to MnPW-H over 100 cycles at low current density. As seen in Fig. S11, the structure disorder remains stable over two cycles of dehydration and rehydration, and a similar amount of interstitial water is captured (MnPW-R2 and R3). Hence, beyond outperforming MnPW-H electrochemical stability, the MnPW-R phase may compete with the rhombohedral phase (MnPW-D) thanks to its structural stability.

Derivative curves of the discharge capacity are illustrated in Fig. 4(c). Different dQ/dV profiles are observed for hydrated and rehydrated compounds. The MnPW-H curve exhibits 3 peaks during charge at 3.37 V, 3.46 V and 3.70 V and 2 peaks during discharge at 3.2 V and 3.57 V. The redox reactions at 3.37–3.46/3.2 V and 3.70/3.57 V can be attributed to LS Fe^{2+}/Fe^{3+} and HS Mn^{2+}/Mn^{3+}[10,30,33,34] The redox reactions of LS Fe^{2+}/Fe^{3+} at ≈3.4 V and HS Mn^{2+}/Mn^{3+} at ≈3.6 V within the range of 2.5–4 V are slightly different from those of the rehydrated sample MnPW-R with 3.44/3.40 V and 3.67/3.57 V, respectively. After the reinsertion of water into the rehydrated sample, the redox reactions of low-spin Fe^{2+}/Fe^{3+} may partially activate, which can be seen at ≈3.4 V for MnPW-R and 3.3 V for MnPW-H.[33] This phenomenon could be linked with a general smaller amount of water for MnPW-R. The MnPW-D curve exhibits one sharp oxidation peak at 3.55 V in the first charge process. However, as observed with the galvanostatic curve of MnPW-D, the reduction peak at 3.45 V becomes larger during discharge with a second reduction peak observed at 3.4 V. This additional peak during discharge can be attributed to residual water in the structure, which is in agreement with the TGA curve (Fig. 3(b)) exhibiting a small amount of water. The presence of water may also lead to a higher polarization of MnPW-H and MnPW-R, in comparison to MPW-D exhibiting a high polarization of 0.1 V.

In order to demonstrate the effect of the water molecules on Na^+ transport, the rate capability performance was evaluated at different current densities (Fig. 4(d)). The specific discharge capacity is plotted as a function of the cycle number to assess

the electrochemical behaviour under various charge–discharge conditions (C/10, C/5, C, and 5C). For the three samples, despite their good capacity retention at C/10, the capacity decreases abruptly at C and 5C. Additionally, MnPW-H exhibits lower capacity retentions over 5 cycles above C/10, in comparison to MnPW-R (89% *vs.* 95% for C/10, 95% *vs.* 98% for C/5, and 95% *vs.* 98% for C). Compared to MnPW-D, the MnPW-R sample shows similar rate capability for different C-rates, such as 95%, 98%, and 98% for C/10, C/5, and C, respectively. Overall, these results confirm that MnPW-R exhibits more stable electrochemical performance over a range of four current densities than MnPW-H. This statement reinforces the hypothesis of the effect of the lower amount of interstitial water in the MnPW-R sample, observed in the TGA analyses. Additional electrochemical characterization studies were performed to strengthen the insight into the influence of water content on the structure. GITT and EIS analyses are presented in the SI (Fig. S12 and S13, respectively) to analyse the solid diffusion kinetics and the charge transfer resistance of MnPW-H, MnPW-D and MnPW-R. The curves of the GITT depending on the capacity and the time in the first charge and discharge cycle of MnPW-H, MnPW-D and MnPW-R are presented in Fig. S12(a and b). Two plateaus at 3.4 V and 3.6 V are visible during the first charge for the hydrated and rehydrated samples, while MnPW-D exhibits one plateau at 3.55 V, corroborating the galvanostatic measurements. A zoomed-in view of the two plateaus is presented in Fig. S12(c and d), and the corresponding D_{Na^+} values of the three samples were calculated. In the first plateau region, MnPW-H, MnPW-D, and MnPW-R exhibit a diffusion coefficient of 6.7×10^{-16} cm^2 s^{-1}, 7.3×10^{-16} cm^2 s^{-1}, and 2.6×10^{-15} cm^2 s^{-1}, respectively. Moreover, a diffusion coefficient of 4.4×10^{-17} cm^2 s^{-1}, 2.0×10^{-16} cm^2 s^{-1}, and 6.3×10^{-17} cm^2 s^{-1} are determined for MnPW-H, MnPW-D and MnPW-R, respectively. Globally, the MnPW-H and MnPW-R diffusion coefficient values are higher in the first plateau region than in the second one, indicating a higher Na^+ diffusion kinetics when the charge begins. This second plateau would probably correspond to the water molecule removal and might explain the poor retention capacity in comparison to the literature.[10,27]

EIS spectra were collected for MnPW-H, MnPW-D, and MnPW-R before cycling, after 1 cycle, and after 5 cycles at C/10 (Fig. S13). Before cycling, MnPW-H electrodes exhibit higher Re(Z) than MnPW-D and MnPW-R even if the values suggest that it is dominated by the contribution of sodium metal (Fig. S13(a)). After the first and 5 cycles, the three samples show a significant increase in impedance, but MnPW-D and MnPW-R impedance values remain lower than that of MnPW-H, indicating increasing interfacial/SEI resistance and impeded Na^+ transport for MnPW-H (Fig. S13(b and c)). Overall, Fig. S13 shows that the presence of water in MnPW-H increases the charge transfer resistance, thereby elevating the overpotential of the material.

Considering the electrochemical performance, the dehydrated compound is competitive in terms of first specific discharge capacity (145 mAh g^{-1} at 0.1C). However, the material demonstrates capacity retention values below those reported in the literature. For example, Song *et al.* studied the electrochemical performance of a $Na_{2-\delta}MnFe(CN)_6 \cdot zH_2O$ compound at 0.7C, reporting 75% capacity retention after 500 cycles.[10] Li *et al.* synthesized a $Na_{1.95}Mn[Fe(CN)_6]_{0.91} \cdot \square_{0.09} \cdot 0.08H_2O$ compound with a reversible capacity of 157 mAh g^{-1} at C/10 in a voltage range of 2.0–4.0 V *vs.* Na/Na^+.[27] Clavelin *et al.* studied electrochemical performance of a dried PW $Na_{1.87}Mn[Fe(CN)_6]_{0.99} \cdot 1.99H_2O$ sample exhibiting a high specific capacity of 154 mAh g^{-1} (90% of the theoretical capacity) while the hydrated compound presents an inferior specific capacity (125 mAh g^{-1}). Furthermore, the capacity retention observed over 20 cycles at C/10 was 77%.[24] In this work, the sodium and $Fe(CN)_6$ content of the initial compound (Na = 1.67, $\square$ = 0.88) is lower than that reported in the literature. The poor retention capacity of the three samples may be explained by the lack of 10% of $Fe(CN)_6$ or the nature of the electrolyte causing unwanted side reactions. Wang *et al.* investigated the electrochemical performance of rehydrated compounds. The compound synthesized in this study is not comparable since iron partially occupies manganese sites. However, for a mostly similar compound, Wang *et al.* showed poor retention capacity (41.5% over 500 cycles) for a rehydrated compound after 10 minutes under ambient air exposure.[18] Hence, differences in rehydration mechanisms can arise from differences in adsorption kinetics, *e.g.* results obtained during the first hour differ from observations made after 24 hours as in our work.

4. Conclusions

The structure of the rehydrated Prussian White compound – a promising Na-ion battery electrode material – measured under ambient air exposure shows the presence of interstitial water in the lattice, which may alter ion insertion mechanisms during the battery cycling process and cause performance losses. Here, we designed *in situ* high resolution synchrotron X-ray diffraction experiments coupled to humidity control to investigate the kinetics of water-induced structural changes in a manganese-based PW $Na_{2-x}Mn[Fe(CN)_6] \cdot yH_2O$ ($0 \leq x \leq 2$) compound as a function of water quantity and establish the atomistic details of the sorption and desorption mechanisms. A controlled rehydration was applied to a dried compound in the rhombohedral phase allowing observation of time-resolved structural evolution. Rietveld refinement analysis was used to extract volume changes and lattice parameter modifications, together with identification of novel phases.

An ultra-fast structure transformation takes place in twenty minutes under the conditions of the experiment, accompanied by the lattice volume expansion and appearance of a new monoclinic phase during the rehydration process. Hence, the rehydration process triggers an irreversible transformation, yielding a disordered monoclinic phase distinct from the as-synthesized material, as reflected in its broader peaks and modified lattice parameters. However, the lattice volume returns to its initial volume after completing the rehydration–dehydration process. A reversible insertion–deinsertion of water molecules is associated with the lattice volume evolution, highlighted by the similar oxygen occupancy and atomic

positions of the hydrated and rehydrated samples after one day under air exposure. Additionally, a reversible rehydration process at the bond scale is demonstrated through ATR-FTIR measurements. SEM observations show the absence of macroscopic alterations. Therefore, the XRD pattern transformation can be attributed to the internal structure (crystal scale) and to structural distortion during the dehydration and rehydration process, which could lead to an irreversible structural change. The lower amount of water filling the interstitial sites of MnPW-R, in comparison to the hydrated one, could be explained by the structural distortions hindering the diffusion of water molecules into the interstitial sites located within the particle core. Regarding the electrochemical performance, promising first discharge capacities of 145 mAh g^{-1} and 112 mAh g^{-1} are obtained for the dried and hydrated PW, respectively, corresponding to 85% and 66% of the theoretical capacity (171 mAh g^{-1}). Surprisingly, MnPW-R and MnPW-D exhibit similar capacity retentions (64% and 61%), while MnPW-H retains only 14% of its initial capacity over 100 cycles at a C/10 rate in a voltage range of 2.5–4 V *vs.* Na^+/Na. The difference in capacity retention values for MnPW-R and MnPW-H could be explained by the structural disorder occurring during the dehydration. The rehydrated monoclinic phase with modified lattice parameters may lead to a more stable phase (Fig. S11). An alternative Na diffusion pathway in the structure might explain the higher capacity retention than MnPW-H over 100 cycles. Hence, this study offers new insights into the impact of heat treatment on structural integrity of MnPW and highlights new pathways for material optimisation to preserve the structure from destabilization under long-term cycling.

Author contributions

The manuscript was written through contributions of all authors. All authors have given approval to the final version of the manuscript. Léna Pineau: conceptualization; methodology; investigation; formal analysis; writing the original draft. David Peralta and Loïc Simonin: conceptualization, supervision, writing, reviewing, and editing. Irina Profatilova: methodology, resources, writing, review, and editing. Yohan Biecher, Quentin Jacquet, and Valentin Vinci: methodology, formal analysis, review, and editing. Sandrine Lyonnard and Jakub Drnec: review, editing, and project administration.

Conflicts of interest

There are no conflicts to declare.

Data availability

All data supporting the findings of this study are provided in the supplementary information (SI) and can be shared upon request after publication. The synchrotron *in situ* X-ray diffraction dataset can be found at https://doi.org/10.15151/ESRF-ES-1901542848. Supplementary information: structural and morphological characterizations of MnPW-H, the methods and tables presenting structural data, and the comparison of structural, morphological and electrochemical characterizations of MnPW-H, MnPW-D and MnPW-R. See DOI: https://doi.org/10.1039/d5ta09250g.

Acknowledgements

Beamtime at the ESRF was granted within the European Battery Hub MA6230. The authors acknowledge Florian Russello for his essential contribution in configuring the beamline setup. The authors also thank Gozde Oney for her valuable assistance with the XRD refinements. The authors are grateful to Martin Clemancey for his help with the Mössbauer analyses and Dane Sotta for his contributions to the KF measurements.

References

1 J.-Q. Huang, R. Du, H. Zhang, Y. Liu, J. Chen, Y.-J. Liu, L. Li, J. Peng, Y. Qiao and S.-L. Chou, *Chem. Commun.*, 2023, **59**, 9320–9335.
2 C. D. Wessells, in *Les Batteries Na-Ion*, ISTE editions, 2021, pp. 297–347.
3 L. Wang, J. Song, R. Qiao, L. A. Wray, M. A. Hossain, Y.-D. Chuang, W. Yang, Y. Lu, D. Evans, J.-J. Lee, S. Vail, X. Zhao, M. Nishijima, S. Kakimoto and J. B. Goodenough, *J. Am. Chem. Soc.*, 2015, **137**, 2548–2554.
4 F. M. Maddar, D. Walker, T. W. Chamberlain, J. Compton, A. S. Menon, M. Copley and I. Hasa, *J. Mater. Chem. A*, 2023, **11**, 15778–15791.
5 X. Shen, X.-Q. Zhang, F. Ding, J.-Q. Huang, R. Xu, X. Chen, C. Yan, F.-Y. Su, C.-M. Chen, X. Liu and Q. Zhang, *Energy Mater Adv*, 2021, **2021**, 2021–1205324.
6 B. Wang, Y. Han, X. Wang, N. Bahlawane, H. Pan, M. Yan and Y. Jiang, *iScience*, 2018, **3**, 110–133.
7 X. Wu, W. Deng, J. Qian, Y. Cao, X. Ai and H. Yang, *J. Mater. Chem. A*, 2013, **1**, 10130.
8 B. Xie, B. Sun, T. Gao, Y. Ma, G. Yin and P. Zuo, *Coord. Chem. Rev.*, 2022, **460**, 214478.
9 G. Goel, M. Sharma and S. K. Tripathi, *J. Energy Storage*, 2025, **126**, 116995.
10 J. Song, L. Wang, Y. Lu, J. Liu, B. Guo, P. Xiao, J.-J. Lee, X.-Q. Yang, G. Henkelman and J. B. Goodenough, *J. Am. Chem. Soc.*, 2015, **137**, 2658–2664.
11 J. Sottmann, F. L. M. Bernal, K. V. Yusenko, M. Herrmann, H. Emerich, D. S. Wragg and S. Margadonna, *Electrochim. Acta*, 2016, **200**, 305–313.
12 C. D. Wessells, R. A. Huggins and Y. Cui, *Nat. Commun.*, 2011, **2**, 550.
13 D. Kim, A. Choi, C. Park, M.-H. Kim and H.-W. Lee, *J. Mater. Chem. A*, 2023, **11**, 13535–13542.
14 Y. Gao, Y. Huang, H. Pan, L. Ji, L. Wang, Y. Tang, Y. Zhu, M. Yan, G. Sun, W. Ni and Y. Jiang, *J. Alloys Compd.*, 2023, **950**, 169886.
15 L. Hartmann, J. Deshmukh, L. Zhang, S. Buechele and M. Metzger, *J. Electrochem. Soc.*, 2023, **170**, 030540.
16 Y. Yang, E. Liu, X. Yan, C. Ma, W. Wen, X.-Z. Liao and Z.-F. Ma, *J. Electrochem. Soc.*, 2016, **163**, A2117–A2123.

17 M. G. Parma, H. Beraldo and I. d. C. Mendes, *ACS Omega*, 2025, **10**, 11375–11385.
18 G. Wang, J. Zheng, K. Zhang, C. Zhang, J. Zheng, W. Fu, J. Wang, J. Li, M. Zhang, L. Meng, J. Wang and Z. Shen, *ACS Nano*, 2025, **19**, 22093–22108.
19 F. Peng, L. Yu, P. Gao, X.-Z. Liao, J. Wen, Y. He, G. Tan, Y. Ren and Z.-F. Ma, *J. Mater. Chem. A*, 2019, **7**, 22248–22256.
20 Y. Lu, L. Wang, J. Cheng and J. B. Goodenough, *Chem. Commun.*, 2012, **48**, 6544.
21 D. O. Ojwang, M. Svensson, C. Njel, R. Mogensen, A. S. Menon, T. Ericsson, L. Häggström, J. Maibach and W. R. Brant, *ACS Appl. Mater. Interfaces*, 2021, **13**, 10054–10063.
22 W. R. Brant, R. Mogensen, S. Colbin, D. O. Ojwang, S. Schmid, L. Häggström, T. Ericsson, A. Jaworski, A. J. Pell and R. Younesi, *Chem. Mater.*, 2019, **31**, 7203–7211.
23 I. Nielsen, D. Dzodan, D. O. Ojwang, P. F. Henry, A. Ulander, G. Ek, L. Häggström, T. Ericsson, H. L. B. Boström and W. R. Brant, *JPhys Energy*, 2022, **4**, 044012.
24 A. Clavelin, D. L. Thanh, I. Bobrikov, M. Fehse, N. E. Drewett, G. A. López, D. Saurel and M. Galceran, *ACS Mater. Lett.*, 2024, **6**, 5208–5214.
25 I.-H. Jo, S.-M. Lee, H.-S. Kim and B.-S. Jin, *J. Alloys Compd.*, 2017, **729**, 590–596.
26 K. Sada, S. M. Greene, S. Kmiec, D. J. Siegel and A. Manthiram, *Small*, 2024, **20**, 2406853.
27 Z. Li, Y. Wang, F. Rabuel, M. Deschamps, G. Rousse, O. Sel and J.-M. Tarascon, *Energy Storage Mater.*, 2025, **76**, 104118.
28 S. N. Ghosh, *J. Inorg. Nucl. Chem.*, 1974, **36**, 2465–2466.
29 J.-H. Lee, J.-G. Bae, M. S. Kim, J. Y. Heo, H. J. Lee and J. H. Lee, *ACS Nano*, 2024, **18**, 1995–2005.
30 P. Xiao, J. Song, L. Wang, J. B. Goodenough and G. Henkelman, *Chem. Mater.*, 2015, **27**, 3763–3768.
31 H. Yao, Y. Gao, X. Lin, H. Zhang, L. Li and S. Chou, *Adv. Energy Mater.*, 2024, 2401984.
32 W. Li, C. Han, W. Wang, Q. Xia, S. Chou, Q. Gu, B. Johannessen, H. Liu and S. Dou, *Adv. Energy Mater.*, 2020, **10**, 1903006.
33 W. Wang, Y. Gang, J. Peng, Z. Hu, Z. Yan, W. Lai, Y. Zhu, D. Appadoo, M. Ye, Y. Cao, Q. Gu, H. Liu, S. Dou and S. Chou, *Adv. Funct. Mater.*, 2022, **32**, 2111727.
34 L. Ge, Y. Song, P. Niu, B. Li, L. Zhou, W. Feng, C. Ma, X. Li, D. Kong, Z. Yan, Q. Xue, Y. Cui and W. Xing, *ACS Nano*, 2024, **18**, 3542–3552.